Boosting electrocatalytic nitrate-to-ammonia conversion via plasma enhanced CuCo alloy-substrate interaction

Angjian Wu[a*#], Yimeng Zhou[a#], Jiabao Lv[a#], Delong Zhang[b], Yaqi Peng[a], Qiulin Ye[a], Pengcheng Fu[b], Weitao Wang[c], Xiaoqing Lin[a], Shaojun Liu[a], Mengxia Xu[a, f], Zhifu Qi[d], Songqiang Zhu[d], Wei Zhu[e], Jianhua Yan[a], Xin Tu[c*], Xiaodong Li[a*]

[a] State Key Laboratory of Clean Energy Utilization, Zhejiang University, Hangzhou, 310027, P. R. China

[b] Interdisciplinary Center for Quantum Information, Zhejiang Province Key Laboratory of Quantum Technology and Device, and Department of Physics, Zhejiang University, Hangzhou, P. R. China

[c] Department of Electrical Engineering and Electronics, University of Liverpool, Liverpool L69 3GJ, United Kingdom

[d] Zhejiang Energy Technology Research Institute Co. Ltd., Hangzhou, 311121, P. R. China

[e] State Key Lab of Organic-Inorganic Composites, Beijing University of Chemical Technology, Beijing 100029, China.

[f] Department of Chemical and Environmental Engineering, University of Nottingham Ningbo China, Ningbo 315100, China

*Corresponding authors.

Email addresses: wuaj@zju.edu.cn (A. Wu),

xin.tu@liverpool.ac.uk (X. Tu),

lixd@zju.edu.cn (X. Li)

[#] These authors contributed equally to this work.

Abstract:

Electrocatalytic converting widely distributed nitrate from industrial wastewater into value-added ammonia was proposed as an attractive and sustainable alternative to harvesting green ammonia. Herein, CuCo alloys were facilely synthesized for nitrate conversion, while non-thermal Ar-plasma was employed to enhance the adhesion strength between the electrocatalyst-substrate interface via regulating the surface hydrophobicity and roughness. Based on Ar-plasma treatment, a high ammonia yield rate (5129.29 μg cm^{-2} h^{-1}) was achieved using $Cu_{30}Co_{70}$ electrocatalyst -0.47 V vs. RHE, while nearly 100% of Faradaic efficiency was achieved using $Cu_{50}Co_{50}$ electrocatalyst at -0.27 V vs. RHE (Reversible Hydrogen Electrode). Validated by in-situ spectroscopy and density functional theory calculation, the high activity of CuCo alloy was derived from the regulation of Co to weaken the strong adsorption capacity of Cu and the shift of the d-band center to lower the energy barrier, while Ar-plasma modification promoted the formation of $^{*}NO$ to boost nitrate conversion.

Keywords: Ammonia synthesis; Non-thermal plasma; Nitrate reduction; CuCo alloy electrocatalyst; DFT calculation

Introduction

Ammonia (NH_3) is one of the essential chemicals and base feedstocks, which is industrially produced mainly through the Haber-Bosch process (HBP) via the reaction between N_2 and H_2 ($N_2 + 3H_2 \rightarrow 2NH_3$). With grey H_2 from catalytic steam methane reforming as the precursor, HBP consumed 3-5% of the world's natural gas supply and 1-2% of the global energy, emitting more than 300 million metric tons of CO_2 annually. The huge capital investment of HBP related to sophisticated infrastructures and harsh operating conditions (450-500 ℃, 20-30 MPa) further hampers its deployment in developing countries or remote areas [1-4]. Therefore, environmentally benign alternatives are of interest considering the promises of carbon neutrality and decentralized NH_3 production. Amongst, electrocatalytic N_2 reduction reaction (ENRR) is considered one of the most promising technologies to harvest NH_3, benefits from mild reaction conditions, modular equipment, and effective compatibility with intermittent renewables [5-9]. Nevertheless, the extremely low selectivity and NH_3 yield rate limit commercial development and industrial advancement significantly. For instance, the general faradaic efficiency (FE) of conventional ENRR is typically below 15%, and the yield rate of NH_3 is far lower than the target set by the U. S. Department of Energy (10^{-4} mol cm^{-2} h^{-1}) [10,11]. Moreover, theoretical calculations for common transition-metal catalysts in ENRR further illustrate the dilemma of simultaneously realizing high activity and selectivity, based on the scaling relations of the adsorption energies of intermediates [12].

Compared to the high bonding energy of N_2 ($N \equiv N$, 948 kJ/mol), nitrate has inherent advantages of high aqueous solubility and easy activation of the N=O bond (204 kJ/mol), which is recently proposed as a promising nitrogen source with a higher reaction rate and selectivity for NH_3 production [13-15]. Currently, nitrate was mainly produced by the Ostwald process via the oxidation of NH_3, whilst its overuse in various industrial and agricultural activities might induce serious aqueous pollution as well as acid rain, photochemical smog, and soil damage [16-19]. Compared to directly recycling low-concentration nitrate from industrial wastewater, renewables-driven electrocatalytic nitrate reduction can alleviate the environmental risk load while

providing a sustainable NH_3 production and facilitating the synthesis of NH_3-based macromolecular chemicals (e.g. urea and amines) [20-22]. However, the electrocatalytic nitrate reduction process is still challenging, due to the sluggish and complex eight-electron reaction process. In addition, the competing hydrogen evolution reaction (HER) occupies the active sites on the surface of the electrocatalysts, thus hampering the adsorption of nitrate on catalysts and decreasing the targeted selectivity of NH_3. Therefore, the rational design of electrocatalysts is essential to achieving efficient electrocatalytic nitrate reduction for NH_3 production [23].

Cu-based catalysts have exhibited prominent high activity in nitrate-to-NH_3 reactions and were widely investigated with the advantage of nitrate affinity and HER inhibition [24]. For instance, Fu et al. applied copper nanosheets as an electrocatalyst, achieving a current density of 10 mA cm^{-2} at -0.15 V vs. RHE, with the NH_3 formation rate of 390.1 μg cm^{-2} h^{-1} [25]. To address the prevailing deactivation of Cu-based electrocatalysts due to the strong adsorption of intermediates, various strategies like heteroatoms doping and alloying are proposed [26]. Wang et al. reported the enhanced activity of NH_3 synthesis from nitrate on a $Cu_{50}Ni_{50}$ alloy compared to pure Cu with nearly unit FE [24]. Similarly, cobalt has also demonstrated excellent performance in nitrate/nitrite reduction and was validated to enable tandemly conversion of the adsorbed intermediate from nitrate conversion to NH_3 [27-28]. Besides, the energy band and the center of the d-band were posited to move towards the Fermi level by introducing Co phase into Cu matrix. Thus, we prepared CuCo alloy to optimize the electronic structure and improve the proton/electron transfer, enabling efficient nitrate-to-NH_3 conversion.

To further enhance the overall electrocatalyst performance, non-thermal plasma (NTP) technology was used to optimize the electrocatalyst-substrate interface [29-31]. Woo et al. compared the effect of different plasma treatments on the peel strength of Ni from polyimide, with the purpose to improve the adhesive force of polymer with metals [32]. Yasuhiro et al found that plasma treatment can effectively guarantee the adhesion and long-term reliability of liquid crystalline polyester film [33]. Song et al. revealed that plasma could modify adhesive force between the catalyst particles and the substrate

via material growth mode changing [34]. Furthermore, it was also assumed strengthening the interaction between the electrocatalyst and substrate via plasma may decrease the contact resistance and decrease the potential drop across the electrocatalytic reaction system.

In this study, CuCo alloy was prepared via facile electrodeposition on an NTP-modified carbon substrate. The effect of various operating parameters (the electrodeposition time, nitrate concentration, potential, Cu/Co ratios, pH and plasma treatment) were systematically investigated in terms of nitrate-to-NH_3 activity. To verify the origin of NH_3, ^{15}N isotope tracing experiments combined with ^{1}H Nuclear Magnetic Resonance (NMR) test were performed. Electrochemical evaluation, density functional theory (DFT) calculation, and in-situ Fourier Transform infrared spectroscopy (FTIR) spectroscopy were performed to reveal the effect of Ar-plasma treatment on the electrocatalyst-substrate interaction as well as the performance of nitrate-to-NH_3 conversion. As a result, a high NH_3 yield rate of 5129.29 μg cm^{-2} h^{-1} was obtained using $Cu_{30}Co_{70}$ electrocatalyst at -0.47 V vs. RHE with Ar-plasma treated carbon substrate, while nearly unity FE was achieved using $Cu_{50}Co_{50}$ electrocatalyst at -0.27 V vs. RHE.

Experimental setup and method

Materials synthesis

All catalysts were prepared via electrodeposition in a typical three-electrode cell with a carbon substrate (1×1 cm^2) as the working electrode, a platinum plate as the counter electrode, and a saturated calomel electrode (SCE) as the reference electrode. 0.05 M H_2SO_4 (Aladdin Ltd) solutions containing 20 mM $CuSO_4$ + Co_2SO_4 (Aladdin Ltd) were used as the deposition baths. The Cu/Co ratio of the CuCo alloy catalysts was controlled by adjusting the ratio of $CuSO_4$/Co_2SO_4. Carbon paper (SGL Carbon Corporate) was used as a substrate and current collector. The electrodeposition was conducted at a current density of 200 mA/cm^2 for 300 seconds. The as-prepared electrodes of Cu/Co alloy were rinsed by deionized water (18 MΩ) and then dried in an N_2 atmosphere overnight for the subsequent electrocatalysis. Herein, the electrocatalyst

CuCo alloys were labeled as $Cu_{80}Co_{20}$, $Cu_{50}Co_{50}$, and $Cu_{30}Co_{70}$, according to the Cu/Co ratios in the deposition solutions which were set at 80/20, 50/50, and 30/70, respectively. To enhance the adhesion between the electrocatalyst and carbon substrate, inductively coupled plasma (ICP) was used to treat the pristine substrate using a 13.56 MHz power source (Kmate, Hero). The pressure of the ICP reactor chamber was evacuated to 10 mTorr using a rotary pump (KYKY, RVP-2). Ar (20 mL/min) was introduced into the reactor by a mass flow controller (MFC). The plasma power of the ICP system was set at 300 W, and the treatment time was set at 5 min, followed by a natural cooling process to room temperature.

Material characterization

The crystal structures of the samples were characterized via X-ray Diffraction (XRD) with the D/max-2550 at room temperature. Scanning electron microscopy (SEM) (Hitachi SU-8010) and transmission electron microscopy (TEM) (Hitachi HT-7700) were employed to investigate the morphology of the samples before and after Ar-plasma modification. The surface compositions of the electrocatalysts were analyzed by X-ray photoelectron spectroscopy (XPS) (ESCALAB 220i-XL Thermo) with Al Ka source of 1486.6 eV. Atomic force microscopy (AFM, Dimension Icon, Bruker Nano INC) was used to estimate the roughness change of carbon substrate induced by plasma treatment. Super-resolution infrared imaging was performed by a mid-infrared photothermal (MIP) imaging and spectroscopy platform (mIRage, Photothermal Spectroscopy Corp.), which was used for morphological and compositional characteristics of prepared alloy electrocatalyst (See details in **Supplementary Note 1**). In situ Fourier-transform infrared spectroscopy (FTIR) was performed using a Nicolet iS50 equipped with a mercury cadmium telluride detector. The reference spectrum was collected at -0.8 V. The spectra were given in absorption units defined as $A = -\log(R/R0)$, where R and R0 represent the reflected IR intensities corresponding to the sample- and reference-single beam spectrum, respectively (See details in **Supplementary Note 2**).

Measurement of NH_3 synthesis

The activities of prepared electrocatalysts were evaluated in a typical three-electrode system using an H-type electrolytic cell. 50 mL of 1M KOH solution was used as the electrolyte, while 0.1 M KNO_3 was added as a precursor. The Nafion proton exchange membrane (PEM) was used to separate the two chambers. The platinum plate was used as the counter electrode, Ag/AgCl was used as the reference electrode, and the working electrode was prepared via the aforementioned method with a size of 1 cm×1 cm. Ar was continuously purged into the electrolyte to eliminate the interference of the background gas, and the potentiostat test method (i-t) was performed for 1h at each operation condition. All the experiments were repeated to maintain reproducibility.

The NH_3 quantification was spectrophotometrically determined by the indophenol blue method (See details in **Supplementary Note 3**). To calculate the NH_3 concentration, the concentration-absorbance curve was calibrated using the standard ammonia chloride solution indicated in **Fig. S1**. NH_3 yield rate was calculated via the equation as follows:

$$Y_{NH_3} = c_{NH_3} \times V/t \qquad (1)$$

where Y_{NH_3} was the NH_3 yield rate; c_{NH_3} was the measured NH_3 concentration; V was the volume of electrolyte; t was the reaction time during electrocatalysis.

FE was calculated according to the following equation:

$$FE = \frac{n \times V_{catholyte} \times c_{NH_3} \times F}{i \times t} \qquad (2)$$

where i is the total current; n represents the number of electron transfers towards the formation of 1 molecule of ammonia, which is 8 for nitrate reduction; $V_{catholyte}$ is the volume of catholyte (mL); c_{NH_3} represents the concentration of ammonia (M); F is the Faraday constant (96485 C mol^{-1}); t is the electrolysis time.

To exclude the influence of N-source from the environment, ^{15}N isotope labeling experiment was performed combined with ^{1}H NMR (600 MHz, Agilent Technologies) test, which can also validate the accuracy of the indophenol blue method for NH_3 quantification. KNO_3-^{15}N (Macklin, >98.5%) was utilized as the nitrogen source, and $^{15}NH_4Cl$ was utilized to calibrate the standard curve. The NH_4^+ product with KNO_3-^{15}N

nitrogen source was tested to confirm the source of nitrogen in ammonia by comparison with the $^{14}NH_4^+$ peak. Then, calibration was performed by preparing a series of standard $^{15}NH_4^+$concentrations (200-1000 ppm) to quantitatively measure ammonia and verify the accuracy of the indophenol blue method. During each test, 40 ml of the solution (after the electrocatalysis process) was extracted to be measured and adjusted the pH to 2-3, followed by mixing with 100 ppm of maleic acid as an internal standard. Adding 0.5 ml of the above solution to 50μl D_2O for NMR testing.

DFT calculation

The calculations were calculated in the "Vienna ab initio simulation package" (VASP) within the framework of density functional theory (DFT). Perdew–Burke–Ernzerhof (PBE) exchange-correlation functional was used to calculate the adsorption energies. To simulate the reaction on the surface of the catalyst, the supercell was used with a vacuum layer of 15 Å. Brillouin zone was accomplished by 3×3×1 Monkhorst-Pack k-point mesh for the systems. The plane-wave was considered with the energy cutoff at 400 eV. The long-range dispersion interaction was described by the DFT-D3 method. The convergence criteria for the total energy and the Hellman-Feynman force are 10^{-5} eV and 0.02 eV $Å^{-1}$, respectively. Gibbs free energy for the elemental steps was calculated by the following equation:

$$G = E + E_{ZPE} - T\Delta S \quad (3)$$

E, E_{ZPE}, T, and S were defined as the DFT total energy, zero-point energy, absolute temperature (298.15 K), and entropy, respectively. VASPKIT was used to calculate zero-point energy and entropy of the intermediates.

Results and discussion

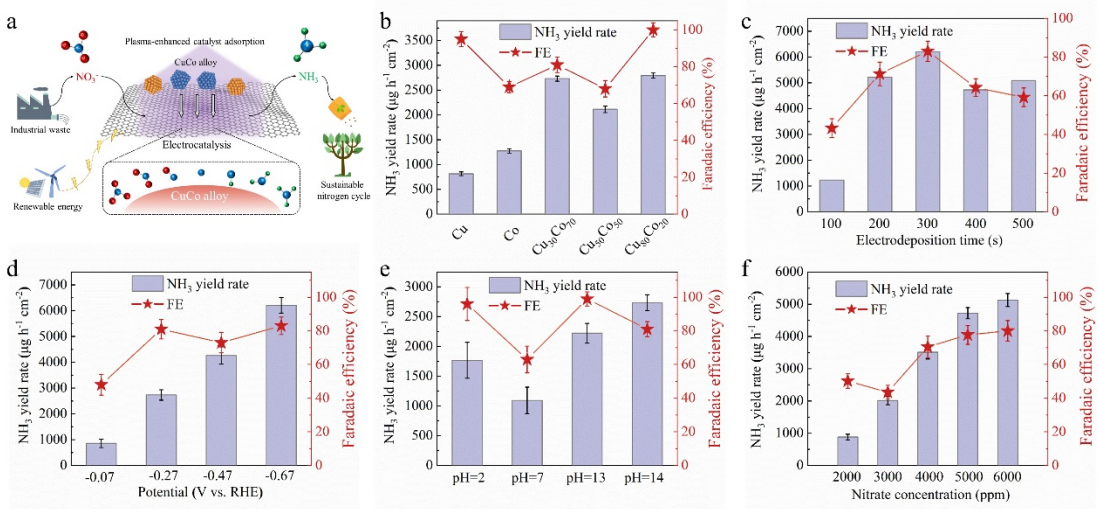

Figure 1. (a) Plasma-enhanced substrate for CuCo-catalyzed NO_3RR mechanism. **(b)** The effect of Cu/Co ratio on the NH_3 yield rate and FE using the CuCo alloy catalyst at -0.27 V vs. RHE. **(c)** the effect of electrodeposition time on the NH_3 yield rate and FE. **(d)** The effect of potential on the NH_3 yield rate and FE using the $Cu_{80}Co_{20}$ catalyst. **(e)** The effect of pH on the NH_3 yield rate and FE at -0.27 V vs. RHE. (f) the effect of nitrate concentration on the NH_3 yield rate and FE at -0.67 V vs. RHE.

To evaluate the electrocatalytic activity, different pH values, potentials and Cu/Co ratios were systematically investigated in a typical H-type cell, as demonstrated in **Fig. 1a**. Compared to pure Cu and Co, CuCo alloy exhibited a significant increase of the reaction activity in terms of NH_3 yield rate and FE, regardless of the Cu/Co ratios (**Fig. 1b**). To confirm the optimum electrodeposition time, we adjusted the electrodeposition time from 100 s to 500 s. It was observed that NH_3 yield rate and FE increased significantly when the electrodeposition time increased from 100 s (1233.96 μg cm^{-2} h^{-1}, 43.2%) to 300 s (6205.28 μg cm^{-2} h^{-1}, 83.0%). However, a further increase of the electrodeposition time will deteriorate the reaction performance, with that NH_3 yield rate and FE decreased to 5092.12 μg cm^{-2} h^{-1} and 59.2% at 500 s, respectively. (**Fig. 1c**). At -0.27 V vs. RHE, the highest NH_3 yield rate of 2793 μg cm^{-2} h^{-1} was achieved with nearly 100% FE using the $Cu_{80}Co_{20}$ electrocatalyst. However, $Cu_{50}Co_{50}$ exhibited inferior activity compared to $Cu_{30}Co_{70}$ and $Cu_{80}Co_{20}$. When negative shifting the

potential from -0.07 vs. RHE to -0.67 V vs. RHE (**Fig. 1d**), the NH_3 yield rate increased almost linearly from 853 μg cm^{-2} h^{-1} to 6205 μg cm^{-2} h^{-1}. Moreover, CuCo alloy exhibited a relatively high NH_3 yield rate and FE (>80%) for acid (pH=2) and base environment (pH=13, 14), while the reaction activity dropped sharply at the neutral electrolyte phosphate buffer saline (PBS) as shown in **Fig. 1e**. The performance of the catalyst was also investigated for different concentrations of nitrate (**Fig. 1f**). The NH_3 yield rate increased monotonically with a higher concentration, from 879.64 μg cm^{-2} h^{-1} at 2000 ppm to 5129.29 μg cm^{-2} h^{-1} at 6000 ppm. Considerable FE (～80%) were achieved at nitrate concentrations above 4000 ppm. To investigate the performance of the catalyst at low nitrate concentrations, we carried out the measurement at concentrations close to underground water (100, 200, 400, and 800 ppm). Figure S2 exhibited a trend of increasing NH3 yield rate from 362.85 μg cm-2 h-1 at 100 ppm to 783.95 μg cm-2 h-1 at 800 ppm with higher concentrations. Compared to ~80% FE above 4000 ppm, the FE was greatly suppressed in low concentrations environments (22% at 800 ppm, ~10% at 100 ppm to 400 ppm). Therefore, the catalyst is more prone to apply in nitrate-enriched wastewater.

By measuring the by-products, we detected H_2 dominated due to the competitive HER, along with trace amounts of NO_2^-. It was observed HER was suppressed and the FE of ammonia promoted from 48% (-0.27 V vs. RHE) to 83% (-0.67 V vs. RHE) by increasing the reduction potential, and a slight change of the FE of nitrite was observed with its value fluctuating between 1% and 3%. (**Fig. S3**) [35]. In addition, the concentrations of the ions in the electrolyte such as ammonia, nitrate and nitrite were also investigated during the nitrate-to-NH_3 conversion process. It was observed that NH_3 was accumulated monotonically during the reaction combined with the continuous consumption of nitrate ions, while little nitrite was produced and its concentration was almost unchanged (**Fig. S4**).

During the preparation of the CuCo alloy catalysts, metal shedding was observed (**Fig. S5**), which implied a relatively weak adhesion of the electrocatalyst to carbon. It was assumed the weak CuCo alloy-substrate interaction might cause large contact resistance and increase the voltage drop across the substrate-electrocatalyst interface.

Non-thermal plasma, widely employed for modifying the surface characteristics (such as roughness, functional group and hydrophobicity), was employed to increase the adhesive force between carbon substrate and CuCo alloy [36]. By comparing three types of carrier gases (Air, Ar, and N_2), electrocatalyst with Ar-plasma modified substrate outperformed the counterparts as shown in **Fig. S6**. Different from the air or N_2 plasma that is normally used to introduce oxygen- or nitrogen-contained radicals and components into the electrocatalyst, Ar-plasma was prone to change the physical roughness and hydrophobicity.

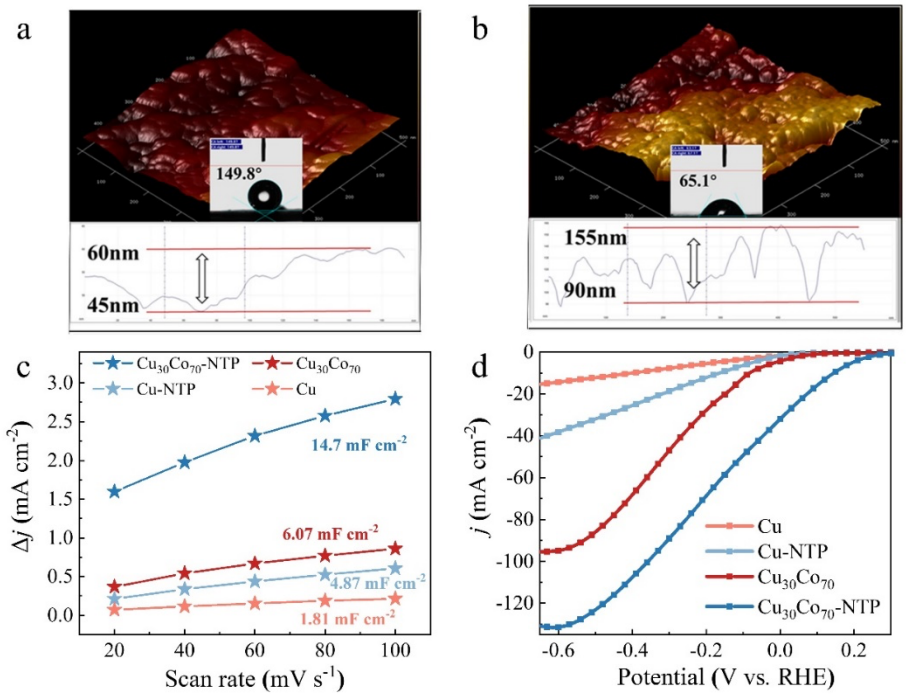

Figure 2. Contact angle measurement and AFM images of carbon substrate **(a)** without and **(b)** with Ar-plasma treatment; **(c)** Comparison of ECSAs using different electrocatalysts (pure Cu, Ar-plasma modified Cu (Cu-NTP), $Cu_{30}Co_{70}$, and Ar-plasma modified $Cu_{30}Co_{70}$ ($Cu_{30}Co_{70}$-NTP)); **(d)** LSV curves of nitrate reduction on the different electrocatalysts (pure Cu, Cu-NTP, $Cu_{30}Co_{70}$, and $Cu_{30}Co_{70}$-NTP) in 0.1 M KNO_3 electrolyte without iR compensation.

Based on contact angle measurements in **Fig. 2a-b**, the pristine carbon substrate was hydrophobic with the contact angle of 149.8°, while it turned into hydrophilic with the contact angle of 65.1° after Ar-plasma treatment (300 W) for 5 mins. Similarly, the

AFM topography images also demonstrated that Ar-plasma treated carbon substrate was much rougher with the occurrence of dense peaks and valleys, compared to the relatively flat surface of the pristine carbon substrate. It was speculated that the plasma modification might remove weak boundaries and introduce undulation on the surface, contributing to the increase of the specific surface area and more anchoring sites. To get insight into the strengthened interaction of catalyst-substrate surface, we compared the electrochemically active surface area (ECSA) of different electrocatalysts by measuring the double-layer capacitances (C_{dl}) in **Fig. 2c** and **Fig. S7**. The $Cu_{30}Co_{70}$-NTP and pure Cu-NTP substrate indicated a larger C_{dl} of 14.7 mF cm^{-2} and 4.87 mF cm^{-2}, respectively, compared to counterparts without plasma modification. It was assumed that active species in Ar-plasma (such as energetic electrons and Ar metastable molecules) will roughen the carbon surface by breaking the chemical bonds via bombardment. Then, the radicals on the surface could re-bond to form a cross-linked network structure, enhancing the interaction between the substrate and the catalyst [37-38]. After Ar-plasma modification, CuCo alloy exhibited an effective and homogeneous adherence to the carbon substrate (**Fig. S8**). On the other hand, optimizing the substrate-catalyst interface via Ar-plasma modification might contribute to a lower resistance (derived from the change of polaron hopping barrier and charge-transfer resistance) and higher surface activity (derived from the change of Gibbs free energy and double-layer capacitance), resulting into better activity for nitrate electro-conversion [39]. As shown in **Fig. S9**, electrochemical impedance spectroscopy (EIS) measurements were performed and fitted to an equivalent circuit model, where the semicircle represented the charge transfer resistance (R_{ct}) at the catalyst surface. After the Ar-plasma treatment, the R_{ct} of the electrocatalyst was reduced from 24.57 Ω to 18.65 Ω, indicating a significant reduction in the resistance of the electrode-electrolyte interface and the promotion of electron transfer by substrate enhancement. As illustrated in **Fig. 2d**, $Cu_{30}Co_{70}$-NTP exhibited excellent performance of nitrate reduction with an ultralow onset potential, superior to all other electrocatalysts. Under alkaline conditions, only a potential of 0.1 V was required to reach the current density

of 50 mA cm^{-2} over $Cu_{30}Co_{70}$-NTP, while the current density exceeded over 150 mA cm^{-2} at -0.2 V vs. RHE (**Fig. 2c**).

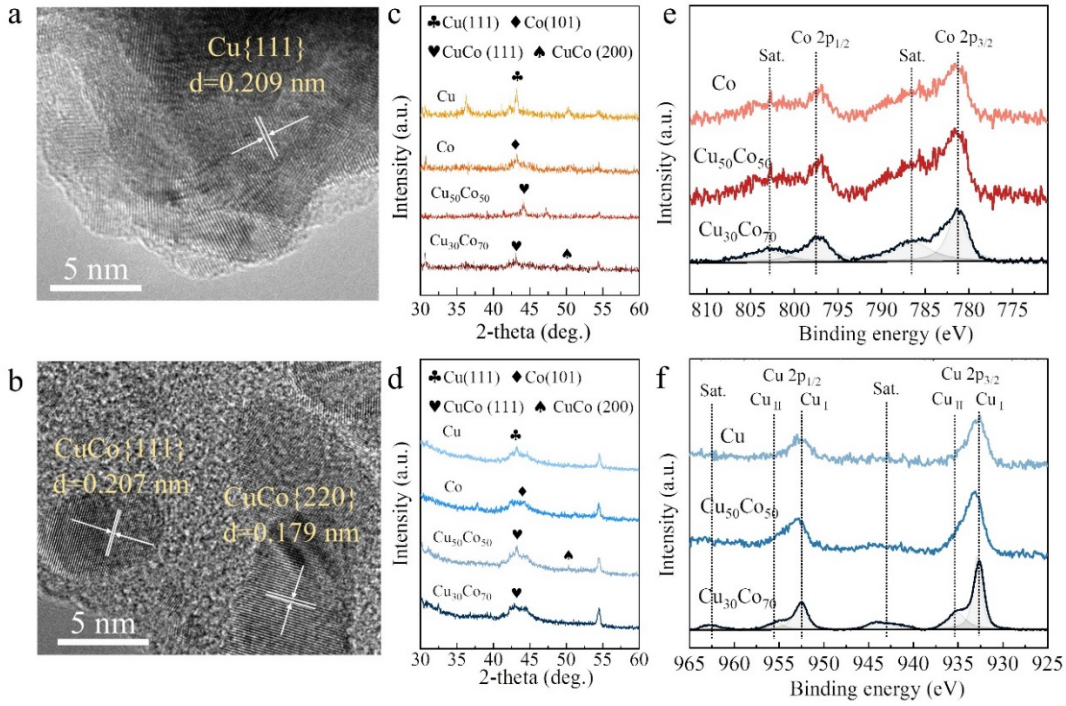

Figure 3. TEM images of **(a)** pure Cu catalyst and **(b)** $Cu_{30}Co_{70}$-NTP. Comparison of XRD patterns of different electrocatalyst deposition on the **(c)** untreated substrate and **(d)** the Ar-plasma treated substrate, respectively. The XPS Cu 2p **(e)** and Co 2p **(f)** spectra of $Cu_{30}Co_{70}$-NTP.

To get insight into the nitrate-to-NH_3 conversion reaction over CuCo alloy surface, the morphology and structure were characterized. In **Fig. 3a-b**, the SEM and TEM images of pristine Cu and $Cu_{30}Co_{70}$-NTP were compared. Different from the dendritic morphologies observed from the pure Cu samples, the growth of spherical $Cu_{30}Co_{70}$ alloy nanoparticles with an average particle size of ~50 nm was observed on Ar-plasma treated substrate. Based on the TEM image (**Fig. S10**), the aggregation of the ellipsoidal alloy particles was observed while EDS mapping demonstrated the homogenous distribution of Cu and Co elements overall the structure (**Fig. S11**). A typical lattice spacing of Cu(111) facets was observed with the lattice space of ~0.209 nm, while the typical lattice spaces of ~0.179 nm and 0.207 nm corresponding to the formation of CuCo(220) and CuCo(111) were observed. In addition, the actual metal loading was

measured by inductively coupled plasma-optical emission spectroscopy (ICP-OES), which demonstrated a CuCo loading ratio (**Table. S1**). As shown in **Fig. 3c-d**, XRD characterization demonstrated the existence of CuCo(111) and CuCo(200) peaks consistent with the observation from the TEM images. And the broader diffraction peaks of $Cu_{30}Co_{70}$-NTP revealed the smaller nanograin sizes generated, which showed better nanocluster dispersion rather than that without plasma treatment. According to XPS spectra, the coexistence of Cu and Co was observed on the Ar-plasma treated substrate (**Fig.3e-f**). Co 2p spectra demonstrated a prominent peak at ~797 eV, which was assigned to Co $2p_{1/2}$. The binding energies at ~781 eV should attribute to the metallic state of Co^0 $2p_{3/2}$. The Cu 2p spectra of $Cu_{30}Co_{70}$ alloy featured peaks at ~952 eV and ~932 eV, which corresponded to the Cu $2p_{1/2}$ and Cu $2p_{3/2}$, respectively [40-42]. Furthermore, compared with $Cu_{50}Co_{50}$ and Cu catalysts, $Cu_{30}Co_{70}$-NTP demonstrated more satellite peaks in Cu 2p energy spectrum, indicating more Cu-Co alloy structure in $Cu_{30}Co_{70}$ [43], which further unveiled the origin of catalyst activity.

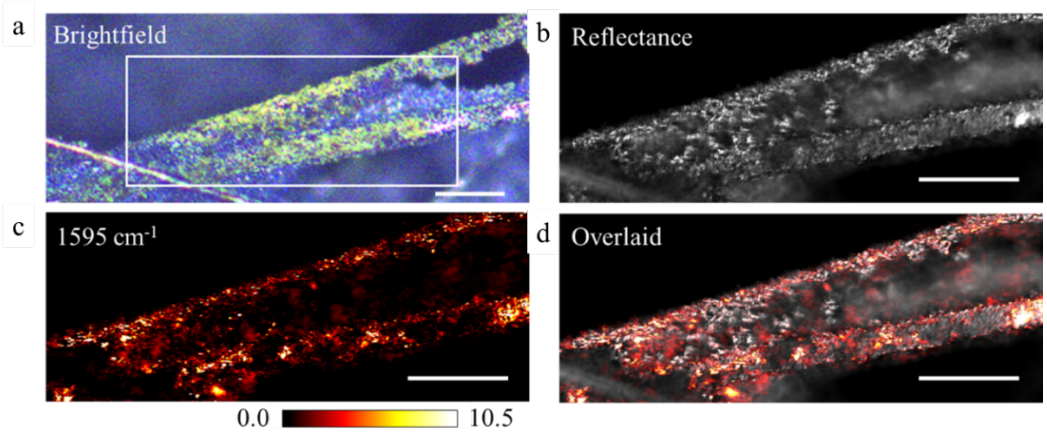

Figure 4. Super-resolution IR imaging characterization of $Cu_{30}Co_{70}$-NTP. **(a)** Brightfield image. **(b)** Reflectance image of the area indicated by the white box in (a) with 532-nm laser illumination. **(c)** Super-resolution IR imaging of the same area by mid-infrared photothermal (MIP) imaging at 1595 cm^{-1} CuCo band. **(d)** Overlay of the reflectance and IR image. Scale bars: 50 μm.

Then, super-resolution infrared (IR) imaging was applied to reveal the intuitive distribution of active CoCu sites at the sub-micrometer scale level. It was realized by a

mid-infrared photothermal (MIP) microscope with sub-micrometer spatial resolution and high IR spectral fidelity [44-46]. In brief, a sub-millimeter field-of-view (FOV) brightfield imaging was performed with white light illumination and visible color Complementary Metal Oxide Semiconductor (CMOS) detector to reveal the corrugated structures of the catalyst substrate **(Fig. 4a-b)**. The region of interest (ROI) of about 240 μm in width, as indicated by the box, was then selected for spectroscopic IR imaging analysis. CuCo alloy-related peak at 1595 cm^{-1} was selected for IR imaging, according to previous studies [47-49]. Prior to MIP imaging, the ROI was confirmed by reflectance imaging of the same probe laser (532 nm, Cobolt Hubner Photonics) (**Fig. 4c**). The images were overlaid for colocalization verification (**Fig. 4d**). Compared to the in-focus areas of the reflectance image, the alloy electrocatalysis sites were observed to equally distribute over the substrate. The macro distribution of CuCo alloy sites also varied in size, ranging from a few hundred nanometers to a few micrometers, indicating a relatively good dispersion of the electrocatalyst over the substrate after Ar-plasma treatment.

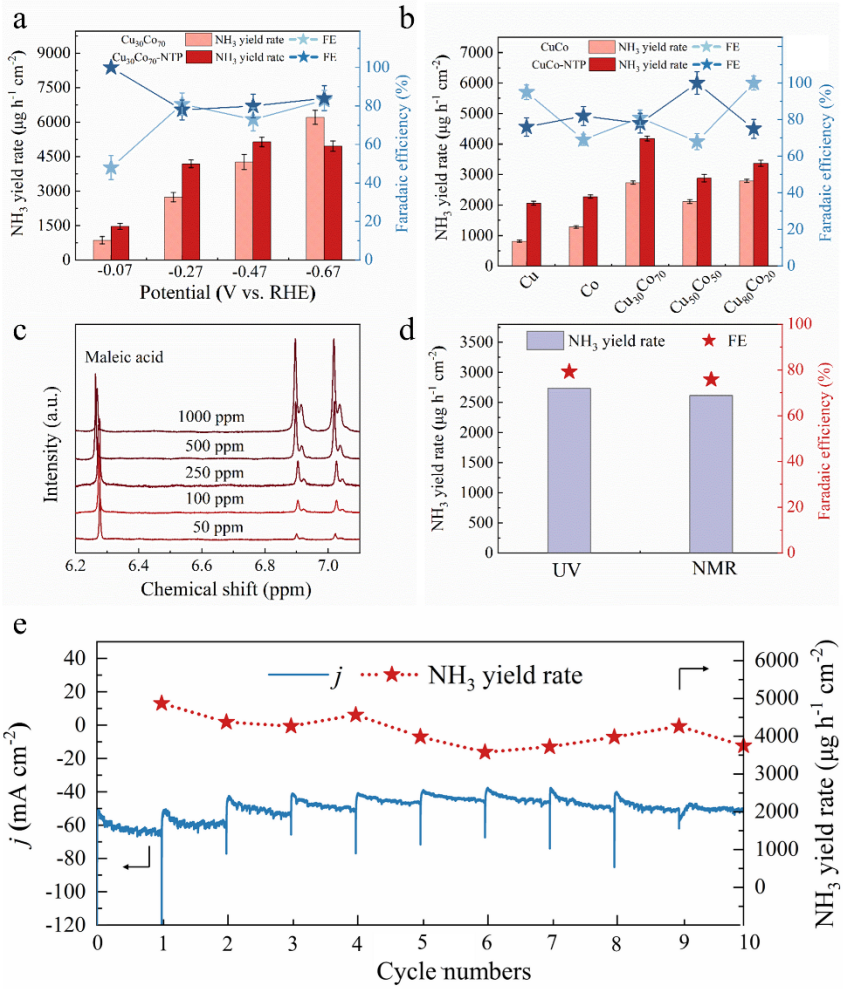

Figure 5. **(a)** The effect of Cu/Co ratio on the NH_3 yield rate and FE at -0.07, -0.27, -0.47, and -0.67 V vs. RHE. **(b)** The effect of potential on the NH_3 yield rate and FE using $Cu_{30}Co_{70}$ and $Cu_{30}Co_{70}$-NTP at -0.27 V vs RHE. **(c)** ^{1}H NMR spectra of ^{15}N-NH_4^+ with different concentrations. **(d)** Comparison of NH_3 production rate and FE by ultraviolet-visible spectroscopy (UV-vis) method and NMR method. **(e)** Stability test of $Cu_{30}Co_{70}$-NTP.

The comparative analysis of nitrate-to-NH_3 activity was investigated in terms of different potentials and Cu/Co ratios, to systematically validate the effect of Ar-plasma modification on the catalyst-substrate interface. As expected, for all Cu/Co ratios, the electrocatalyst with Ar-plasma modification exhibited dramatically increase in NH_3 yield rate (**Fig.5a**). For the Cu/Co ratio of 50:50, the NH_3 yield rate increased by 36% after Ar-plasma treatment, accompanied by an increase of the FE from 68.4% to nearly

100%. The NH_3 yield rate had a distinct enhancement regardless of the potential and pH variation, as depicted in **Fig. 5b** and **Fig. S12**. At −0.47 V vs. RHE, the NH_3 yield rate increased to 5129.29 μg cm^{-2} h^{-1} using Ar-plasma treated substrate without the sacrifice of FE. As shown in **Table S2**, the NH_3 yield rate reported here outperformed most previous nitrate-to-NH_3 conversions over various state-of-the-art electrocatalysts.

On the other hand, to verify that nitrate was the sole N source for ammonia harvest, an isotope labeling experiment was performed. No triplet speaks corresponding to ^{14}N was observed in the solution after electrocatalysis, indicating that nitrate is the only source nitrogen instead of other contaminants. The yield rate of $^{15}NH_4^+$ was quantified by ^1H NMR spectra with external standards of maleic acid. The results further confirmed the accuracy of the spectrophotometric method using the indophenol blue method **(Fig. 5c-d)**.

The long-term stability of the electrocatalyst is also an indicator for evaluating the catalytic performance. A long-term experiment of 10 cycles was performed on $Cu_{30}Co_{70}$ electrocatalyst (**Fig. 5e**), which indicated the current density remained stable together with an almost constant NH_3 yield rate. As shown in **Fig. S13**, SEM and XPS characterization of $Cu_{30}Co_{70}$ electrocatalyst after the long-term reaction (10 h) was performed. For Co_{2p} orbitals, the positions of Co $2p_{3/2}$, Co $2p_{1/2}$ and satellite peaks did not shift, with the peak width and peak height being relatively consistent, which was also verified by the Cu 2p orbital. However, the difference in some satellite peaks was observed in Cu spectra, which might be due to the formation of copper oxides. In addition, no release of metal was observed after the reaction in the electrolyte.

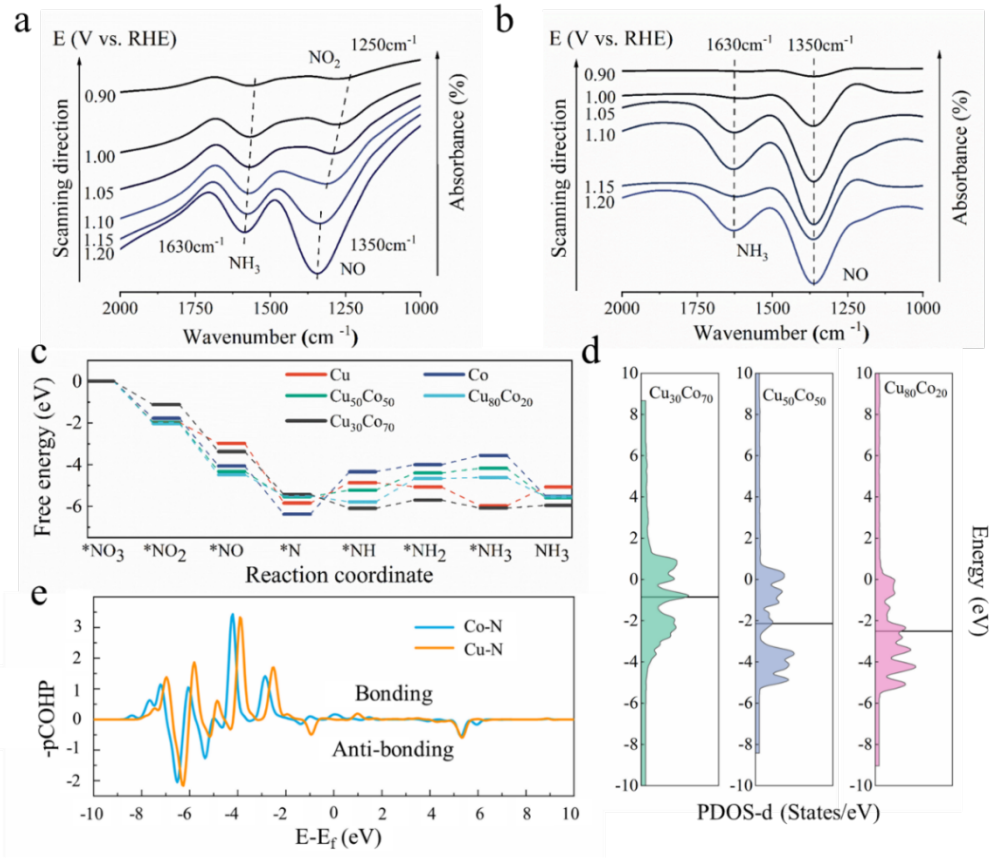

Figure 6. In-situ FTIR spectra of **(a)** the $Cu_{30}Co_{70}$ and **(b)** $Cu_{30}Co_{70}$-NTP via linear scanning in 1M KOH + 0.1 M KNO_3 at different potentials (-0.9~-1.2 V vs. Ag/AgCl) and DFT calculations: **(c)** Free energy diagram with the different reaction pathways on the catalyst surface. **(d)** The partial density of states (PODS) of $Cu_{30}Co_{70}$, $Cu_{50}Co_{50}$, and $Cu_{80}Co_{20}$ alloy. **(e)** Crystal orbital Hamilton population (COHP) for catalyst adsorption of NH_3.

Then, DFT calculation and in-situ FTIR spectroscopy were performed to unravel the reaction pathway and the origin of high nitrate-to-NH_3 activity from CuCo alloy and the effect of Ar-plasma treatment. As shown in the FTIR spectra (**Fig. 6a-b**), the negative bands at ~ 1250 cm^{-1}, corresponding to the intermediates of $^*NO_2$, and H-N-H bend of NH_3 at ~1630 cm^{-1}, were observed during nitrate conversion using $Cu_{30}Co_{70}$ alloy. With the decrease of potential from -0.9 to -1.2 V vs. Ag/AgCl, the shifting of NH_3 bands to large wavenumber was observed, together with the observation of the transformation of NO_2^- band to $^*NO$ band at ~1350 cm^{-1} [50-53]. As for $Cu_{30}Co_{70}$ alloy

with the substrate modified by Ar-plasma, only two obvious bands assigned to NH_3 and NO were observed with the variation of applied potential. Hence, $^*NO$ was assumed as a key intermediate for nitrate conversion and was prone to form after plasma treatment. Considering the different adsorption directions on various adsorption sites, the total energy on the stabilized intermediates over the surface the electrocatalysts was calculated, and the lowest free energy was the most stable configuration of the intermediate (**Fig. S14**). In a typical alkaline (1 M KOH) environment, the reaction process of NH_3 synthesis from nitrate reduction was considered through a series of deoxidation and hydrogenation reactions.

$$NO_3^- + 6H_2O + 8e^- \rightarrow NH_3 + 9OH^- \quad (4)$$

The structural relaxation of CuCo was speculated that Co was prone to replace Cu atoms of subsurface dependent on the thermodynamics so that the nitrate ions were more inclined to bond with Cu on the surface. By calculating the intermediate's free energy at each step, the potential catalytic mechanism was revealed. The deoxygenation reaction spontaneously occurs with CuCo catalysts during the nitrate for NH_3, which corroborated with the observation of more NO species based on in situ FTIR spectra. As indicated in **Fig. 6c**, it can be judged from the energy path that the catalytic deoxidation process of Co was significantly weaker than that of Cu, especially in the $^*NO_3 \rightarrow {}^*NO_2$ process. However, the catalyst poisoning caused by the adsorption of nitrogen oxides hampered Cu to carry out the subsequent reaction. The CuCo-doped catalysts adjusted the NO adsorption and hydro-desorption capacity. The relatively low activity and selectivity of $Cu_{80}Co_{20}$ electrocatalyst originated from a higher energy barrier during the hydrogenation process of $^*NH \rightarrow {}^*NH_2$. With the increase of the doping ratio of Co, the performance of $Cu_{50}Co_{50}$ can be improved to a certain extent attributed to the change of energy barrier, while the performance reaches its peak using $Cu_{30}Co_{70}$ as an electrocatalyst. It was due to the lowest energy difference (0.775 eV) of the rate-determining step (RDS), resulting in high selectivity and high efficiency of catalyzing nitrate to NH_3.

In **Fig. 6d**, the calculation of partial density of states (PDOS) calculation indicated that $Cu_{30}Co_{70}$ alloy possessed a higher d-band center near the Fermi level, which was

~1.28 eV higher than that of $Cu_{50}Co_{50}$ alloy, and ~1.66 eV higher than that of $Cu_{80}Co_{20}$ alloy, respectively. Hence, it pushed the anti-bonding orbital higher than the Fermi level, which was conducive to adsorption. Therefore, the $Cu_{30}Co_{70}$ alloy exhibited a better performance compared to the counterpart electrocatalyst. Cu and Co showed different properties in the last step of ammonia desorption ($^*NH_3 \rightarrow NH_3$), so COHP calculations were performed for Cu-N and Co-N in $^*NH_3$. The COHP value of Cu-N (-3.377 eV) was significantly lower than that of Co-N (-2.976 eV), which reflected that Cu benefited from a stronger adsorption capacity for NH_3 adsorbed species (**Fig. 6e**). It was inferred that the doping of Co could improve the overall performance of the catalyst by optimizing the desorption of NH_3.

Conclusion

In this study, a highly efficient bimetallic CuCo alloy electrocatalyst was designed for NH_3 production from electrochemical nitrate reduction. It was demonstrated that Ar-plasma modification could boost the activity of the electrocatalyst by enhancing the adhesion force between CuCo alloy and carbon substrate. Based on the analysis of ECSA and surface characteristics, we demonstrated that the plasma modification of CuCo alloy changed the hydrophobicity of the carbon substrate. By optimizing the potential and Cu/Co ratio, the NH_3 yield rate of 5129.29 μg cm^{-2} h^{-1} was achieved at -0.47 V (vs. RHE) using $Cu_{30}Co_{70}$ after Ar-plasma treatment. Furthermore, in-situ FTIR spectra confirmed the formation of $^*NO$ and intermediate of NO_2^- during nitrate conversion, while plasma-modification facilitated the generation of NH_3 and N-related intermediates. The DFT revealed that the activity of $Cu_{30}Co_{70}$ was due to the lowest energy difference (0.775 eV) in RDS, with a higher d-band center and the stronger desorption capacity of NH_3. Based on this study, we provided an effective strategy to optimize both interfaces of substrate-electrocatalyst and electrocatalyst-electrolyte to realize efficient NH_3 synthesis from electrocatalytic nitrate conversion.

Acknowledge:

This work is supported by the National Nature Science Foundation of China (51976191, 51806193), the Ecological civilization project, Zhejiang University, the Pioneer R&D Program of Zhejiang Province-China (2022C03040) and the Fundamental Research Funds for the Central Universities (226-2022-00091).

Supporting Information:

Standard curves for product measurements; NH3 yield and FE; variation in nitrogen species concentration in solution; ECSA and EIS measurements; XPS and SEM characterisation of catalysts; performance comparison; DFT models.

References

1. Foster, S. L.; Bakovic, S. I. P.; Duda, R. D.; Maheshwari, S.; Milton, R. D.; Minteer, S. D.; Janik, M. J.; Renner, J. N.; Greenlee, L. F. Catalysts for nitrogen reduction to ammonia. *Nat. Catal.* **2018**, 1, 490-500, DOI 10.1038/s41929-018-0092-7.
2. Lee, H. K.; Koh, C. S. L.; Lee, Y. H.; Liu, C.; Phang, I. Y.; Hang, X.; Tsung, C.; Ling, Y. X. Favoring the unfavored: selective electrochemical nitrogen fixation using a reticular chemistry approach. *Sci. Adv*. **2018**, 4, eaar3208, DOI 10.1126/sciadv.aar3208.
3. Kitano, M.; Kanbara, S.; Inoue, Y.; Kuganathan, N.; Sushko, P. V.; Yokoyama, T.; Hara, M.; Hosono, H. Electride support boosts nitrogen dissociation over ruthenium catalyst and shifts the bottleneck in ammonia synthesis, *Nat. Commun*. 2015, 6, 6731, DOI 10.1038/ncomms7731.
4. Shipman, M. A.; Symes, M. D. Recent progress towards the electrosynthesis of ammonia from sustainable resources. *Catal. Today*. **2017,** 286: 57-68, DOI 10.1016/j.cattod.2016.05.008.
5. Chen, J. G.; Crooks, R. M.; Seefeldt, L. C.; Bren, K. L.; Bullock, R. M.; Darensbourg, M. Y.; Holland, P. L.; Hoffman, B.; Janik, M. J; Jones, A. K.; Kanatzidis, M. G.; King, P.; Lancaster, K. M.; Lymar, S. V.; Pfromm, P.; Schneider, W. F.; Schrock, R. R. Beyond fossil fuel-driven nitrogen transformations. *Science*. **2018**, eaar6611, DOI 10.1126/science.aar6611.

6. Xu, X.; Tian, X.; Sun, B.; Liang, Z.; Cui, H; Tian, J.; Shao, M. 1 T-phase molybdenum sulfide nanodots enable efficient electrocatalytic nitrogen fixation under ambient conditions. *Appl. Catal. B Environ*. **2020**, 272, 118984, DOI 10.1016/j.apcatb.2020.118984.
7. Yang, X.; Sun, S.; Meng, L.; Li, K.; Mukherjee, S.; Chen, X.; Lv, J.; Liang, S.; Zang, H.; Yan, L.; Wu, G. Molecular single iron site catalysts for electrochemical nitrogen fixation under ambient conditions. *Appl. Catal. B Environ*. **2021**, 28, 119794, DOI 10.1016/j.apcatb.2020.119794.
8. Xiao, L.; Zhu, S.; Liang, Y.; Li, Z.; Wu, S.; Luo, S.; Chang, C.; Cui, Z. Effects of hydrophobic layer on selective electrochemical nitrogen fixation of self-supporting nanoporous Mo_4P_3 catalyst under ambient conditions. *Appl. Catal. B Environ*. **2021**, 286, 119895, DOI 10.1016/j.apcatb.2021.119895.
9. Shi, Y.; Liu, Y. Vacancy and N dopants facilitated Ti3+ sites activity in 3D Ti3-xC2Ty MXene for electrochemical nitrogen fixation. *Appl. Catal. B Environ*. **2021**, 297, 120482, DOI 10.1016/j.apcatb.2021.120482.
10. Wang, C.; Gu, L.; Qiu, S.; Gao, J.; Zhang, Y.; Wang, K.; Zou, J.; Zhu, X. Modulating CoFe2O4 nanocube with oxygen vacancy and carbon wrapper towards enhanced electrocatalytic nitrogen reduction to ammonia. *Appl. Catal. B Environ*. **2021**, 297, 120452, DOI 10.1016/j.apcatb.2021.120452.
11. Antonio José Martín, Javier Pérez-Ramírez, Heading to distributed electrocatalytic conversion of small abundant molecules into fuels, chemicals, and fertilizers. *Joule*. **2019**, 3, 2602-2621, DOI 10.1016/j.joule.2019.09.007.
12. Montoya, J. H.; Tsai, C.; Vojvodic, A.; Nørskov, J. K. The challenge of electrochemical ammonia synthesis: a new perspective on the role of nitrogen scaling relations. *ChemSusChem*. **2015**, 8, 2180-2186, DOI 10.1002/cssc.201500322.
13. Cai, J.; Wei, Y.; Cao. A.; Huang, J.; Jiang, Z.; Lu, S.; Zang, S. Electrocatalytic nitrate-to-ammonia conversion with ~100% Faradaic efficiency via single-atom alloying. *Appl. Catal. B-Environ*. **2022**, 316, 121683, DOI 10.1016/j.apcatb.2022.121683

14. Lu, X.; Yu, J.; Cai, J.; Zhang, Q.; Yang, S.; Gu, L.; Waterhouse, G. I. N.; Zang, S.; Yang, B.; Lu, S. Exclusive nitrate to ammonia conversion via boron-doped carbon dots induced surface Lewis acid sites. *Cell Rep. Phys. Sci*. **2022**, 3, 100961, DOI 10.1016/j.xcrp.2022.100961.
15. Lu, X.; Song, H.; Cai, J.; Lu, S. Recent development of electrochemical nitrate reduction to ammonia: A mini review. *Electrochem. Commun*. **2021**, 129, 107094, DOI 10.1016/j.elecom.2021.107094.
16. Davidson, E. A.; David, M. B.; Galloway, J. N.; Goodale, C. L.; Haeuber, R.; Harrison J. A.;, Howarth, R. W.; Jaynes, D. B.; Lowrance, R. R.; Thomas, N. B.; Peel, J. L.; Pinder, R. W.; Porter, E.; Snyder, C. S.; Townsend, A. R.;Ward, M. H. Excess Nitrogen in the U.S. Environment: Trends, Risks, and Solutions. *Issues in Ecology*. **2012**, 12, 1-16. www.esa.org/esa/wp-content/uploads/2013/03/ issuesinecology15.pdf.
17. Duca, M.; Koper, M. T. M. Powering denitrification: the perspectives of electrocatalytic nitrate reduction. *Energy Environ. Sci*. **2012**, 5, 9726-9742, DOI 10.1039/C2EE23062C.
18. Rosca, V.; Duca, M.; Groot, M. T.; Koper, T. M. Nitrogen cycle electrocatalysis. *Chem. Rev*. **2009**, 109, 2209-2244, DOI 10.1021/cr8003696.
19. Seraj, S.; Kunal, P.; Li, H.; Henkelman, G.; Humphrey, S. M.; Werth, C. J. PdAu alloy nanoparticle catalysts: effective candidates for nitrite reduction in water. *ACS Catal*. **2017**, 7, 3268-3276, DOI 10.1021/acscatal.6b03647.
20. Butcher, D. P.; Gewirth, A. A. Nitrate reduction pathways on Cu single crystal surfaces: Effect of oxide and Cl-. *Nano Energy*. **2016**, 29, 457-465, DOI 10.1016/j.nanoen.2016.06.024.
21. Pérez-Gallent, E.; Figueiredo, M. C.; Katsounaros, I.; Koper, M. T. M. Electrocatalytic reduction of nitrate on copper single crystals in acidic and alkaline solutions. *Electrochim. Acta*. **2017**, 227, 77-84, DOI 10.1016/j.electacta.2016.12. 147.

22. Hawtof, R.; Ghosh, S.; Guarr, E.; Xu, C.; Sankaran, R. M.; Renner, J. N. Catalyst-free, highly selective synthesis of ammonia from nitrogen and water by a plasma electrolytic system. *Sci. Adv.* **2019,** 5, eaar:5778, DOI 10.1126/sciadv.aat5778.
23. Singh, A. R.; Rohr, B. A.; Schwalbe, J. A.; Cargnello, M.; Chan, K.; Jaramillo, T. F.; Chorkendorff, I.; Nørskov, J. K. Electrochemical ammonia synthesis-the selectivity challenge. *ACS Catal*. **2017**, 7, 706-709, DOI 10.1016/j.checat.2022.09.001
24. McEnaney, J. M.; Blair, S. J.; Nielander, A. C.; Schwalbe, J. A.; Koshy, D. M.; Cargnello, M.; Jaramillo, T. F. Electrolyte Engineering for Efficient Electrochemical Nitrate Reduction to Ammonia on a Titanium Electrode. *ACS Sustain. Chem. Eng*. **2020**, 7, 2672-2681, DOI 10.1021/acssuschemeng.9b05983.
25. Fu, X.; Zhao, X.; Hu, X.; He, K.; Yu, Y.; Li, T.; Tu, Q.; Qian, X.; Yue, Q.; Wasielewski, M. R.; Kang, Y. Alternative route for electrochemical ammonia synthesis by reduction of nitrate on copper nanosheets. *Appl. Mater.* **2020**, 4, 100620, DOI 10.1016/j.apmt.2020.100620.
26. He, W.; Zhang, J.; Dieckhofer, S.; Varhade, S.; Brix, A. C.; Lielpetere, A.; Seisel, S.; Junqueira. J. R. C.; Schuhmann, W. Splicing the active phases of copper/cobalt-based catalysts achieves high-rate tandem electroreduction of nitrate to ammonia, *Nat. Commun*. 2022, 13, 1129, DOI 10.1038/s41467-022-28728-4.
27. Wang, Y.; Xu, A.; Wang, Z.; Huang, L.; Li, J.; Li, F.; Wicks, J.; Luo, M.; Nam, D.; Tan, C.; Ding, Y.; Wu, J.; Lum, Y.; Dinh, C.; Sinton, D.; Zheng, G.; Sargent, E. H. Enhanced Nitrate-to-Ammonia Activity on Copper-Nickel Alloys via Tuning of Intermediate Adsorption. *J. Am. Chem. Soc*. **2020**, 142, 5702-5708, DOI 10.1021/jacs.9b13347.
28. Cheng, H.; Huang, Y.; Wang, A.; Wang, X.; Zhang, T. Preparation of Cobalt Nitride from Co–Al Hydrotalcite and its Application in Hydrazine Decomposition. *Top Catal.* **2009**, 52, 1535-1540, DOI 10.1007/s11244-009-9294-1.
29. Wang, R.; Ye, B.; Kong, X.; Xia, Z.; Zhang, Z.; Li, H.; Xie, P. Research Progress of Low Temperature Plasma Surface Strengthening Technology. *J. Mech. Eng*. **2021**, 57, 192-207, DOI 10.3901/JME.2021.12.192.

30. Tian, Y.; Ye, Y.; Wang, X.; Peng, S.; Wei, Z.; Zhang, X.; Liu, W. Three-dimensional N-doped, plasma-etched graphene: Highly active metal-free catalyst for hydrogen evolution reaction. *Appl. Catal. A Gen*. **2017**, 529, 127-133, DOI 10.1016/j.apcata.2016.10.021.
31. Zheng, J.; Xu, A.; Wu, A.; Li. X. Plasma-Engraved Co2N Nanostructures toward High-Performance Alkaline Hydrogen Evolution. *ACS Appl. Mater. Interfaces*. **2021**, 18, 13, DOI 10.1021/acsami.1c01698.
32. Woo, T.; Park, I.; Jung, K.; Jeon, W.; Hwang, Y.; Seol, K. Effects of plasma treatment on the peel strength of Ni on polyimide. *Electron. Mater. Lett*. **2012**, 2, 8, DOI 10.1007/s13391-012-1075-5.
33. Kurihara, Y.; Ohata, H.; Kawaguchi, M.; Yamazaki, S.; Kimura, L. Improvement of adhesion and long-term adhesive reliability of liquid crystalline polyester film by plasma treatment. *J. Appl. Polym. Sci.* **2008**, 108, 85-92, DOI 10.1002/app.27537.
34. Song, I. K.; Cho, Y. S.; Choi, G. S.; Kim, D. J. The growth mode change in carbon nanotube synthesis in plasma-enhanced chemical vapor deposition, *Diam. Relat. Mater*. **2004**, 13: 1210-1213, DOI 10.1016/j.diamond.2004.01.006.
35. Li, L.; Cheng Tang, C.; Cui, X.; Zheng, Y.; Wang, X.; Xu, H.; Zhang, S.; Shao, T.; Davey, K.; Qiao, S. Efficient Nitrogen Fixation to Ammonia through Integration of Plasma Oxidationwith Electrocatalytic Reduction. *Angew. Chem. Int. Ed*. **2021**, 60:14131–14137, DOI 10.1002/anie.202104394.
36. Dumitrascu, N.; Topala, I.; Popa, G.; Dielectric barrier discharge technique in improving the wettability and adhesion properties of polymer surfaces, *IEEE Trans. Plasma Sci*. **2005**, 33,1710-1714, DOI 10.1109/TPS.2005.856335.
37. Zhou, P.; He, J.; Zou, Y.; Wang, Y.; Xie, C.; Chen, R.; Zang, S.; Wang, S. Single-crystalline layered double hydroxides with rich defects and hierarchical structure by mild reduction for enhancing the oxygen evolution reaction. *Sci China Chem*. **2019**, 62, 1365-1370, DOI 10.1007/s11426-019-9511-x.

38. Rosenberg, M.; Sheehan, D. P.; Petrie, J. R. Use of dusty plasmas for surface-enhanced vibrational spectroscopy studies. *J. Phys. Chem. A*. **2004**, 108, 5573-5575, DOI 10.1021/jp0347365.
39. Wu, A.; Yang, J.; Xu, B.; Wu, X.; Wang, Y.; Lv, X.; Ma, Y.; Xu, A.; Zheng, J.; Tan, Q.; Peng, Y.; Qi, Z.; Qi, H.; Li, J.; Wang, Y.; Harding, J.; Tu, X.; Wang, A.; Li, X. Direct ammonia synthesis from the air via gliding arc plasma integrated with single atom electrocatalysis. *Appl. Catal. B* Environ. **2021**, 8, 120667, DOI 10.1016/j.apcatb.2021.120667.
40. Xu, A.; Dong, C.; Wu, A.; Li, R.; Wang, L.; Macdonald, D. D.; Li, X. Plasma-modified C-doped Co_3O_4 nanosheets for the oxygen evolution reaction designed by Butler-Volmer and first-principle calculations. *J. Mater. Chem. A*. **2019**, 7, 4581-4895, DOI 10.1039/C8TA11424B.
41. Shui, S.; Huang, C.; Ma, P.; Li, W.; He, Q.; Wu, W.; Tan, Y.; Bao, J. Accelerating C2+ alcohols synthesis from syngas by simultaneous optimizations of CO dissociation and chain growth over CuCo alloy catalyst. *Chin Chem Lett.* **2021**, 32, 2203-2206, DOI 10.1016/j.cclet.2020.12.022.
42. Gao, W.; Zhao, Y.; Chen, H.; Chen, H.; Li, Y.; He, Shan.; Zhang, Y.; Wei, M.; Evans, D. G.; Duan, X. Core–shell Cu@(CuCo-alloy)/Al_2O_3 catalysts for the synthesis of higher alcohols from syngas. *Green Chem*. **2015**, 17, 1525-1534, DOI 10.1039/C4GC01633E.
43. Noh, H.; Lee, K.; Chandra, P.; Won, M.; Shim, Y.; Application of a Cu–Co alloy dendrite on glucose and hydrogen peroxide sensors. *Electrochim*. **2012**, 61, 36-43.
44. Zhang, D.; Li, C.; Zhang, C.; Slipchenko, M. N.; Eakins, G.; Cheng, J. Depth-resolved mid-infrared photothermal imaging of living cells and organisms with submicrometer spatial resolution. *Sci. Adv*. **2016**, 2, 9, DOI 10.1016/j.electacta.2011.11.066.
45. Li, C.; Zhang, D.; Slipchenko, M. N.; Cheng, J. Mid-Infrared Photothermal Imaging of Active Pharmaceutical Ingredients at Submicrometer Spatial Resolution. *Anal. Chem*. **2017**, 9, 89, DOI 10.1021/acs.analchem.6b04638.

46. Su, Y.; Hu, X.; Tang, H.; Lu, K.; Li, H.; Liu, S.; Xing, B.; Ji, R. Steam disinfection releases micro(nano)plastics from silicone-rubber baby teats as examined by optical photothermal infrared microspectroscopy. *Nat. Nanotechnol*. **2022**, 17, 76-85, DOI 10.1038/s41565-021-00998-x.
47. Klementieva, O.; Sandt, S.; Martinsson, I.; Kansiz, M.; Gouras, G. K.; Borondics, F. Super-Resolution Infrared Imaging of Polymorphic Amyloid Aggregates Directly in Neurons. *Adv. Sci.* **2020**, 6, 7, DOI 10.1002/advs.201903004.
48. Wang, D.; He, N.; Xiao, L.; Dong, F.; Chen, W.; Zhou, Y.; Chen, C.; Wang, S. Coupling electrocatalytic NO oxidation over carbon cloth with hydrogen evolution reaction for nitrate synthesis. *Angew. Chem. Int. Ed*., **2021**, 60, 24810-24816, DOI 24605-2461, 10.1002/ange.202109905.
49. Wu, Z.; Karamad, K.; Yong, X.; Huang, Q.; Cullen, D. A.; Zhu, P.; Xia, C.; Xiao, Q.; Shakouri, M.; Chen, F.; Kim, J. Y.; Xia, Y.; Heck, K.; Hu, Y.; Wong, M. S.; Li, Q.; Gates, I.; Siahrostami, S.; Wang, H. Electrochemical ammonia synthesis via nitrate reduction on Fe single atom catalyst. *Nat. Commun*. **2021**,12, 2870, DOI 10.1038/s41467-021-23115-x.

    Hu, C.; Zhang, L.; Li, L.; Zhu, W.; Deng, W.; Dong, H.; Zhao, Z.; Gong, J. Theory assisted design of N-doped tin oxides for enhanced electrochemical CO_2 activation and reduction. *Sci China Chem*. **2019**, 62: 1030-1036, DOI 10.1007/s11426-019-9474-0.
50. Figueiredo, M. C.; Solla-Gullón, J.; Vidal-Iglesias, F J.; Climent, V.; Feliu, J. M. Nitrate reduction at Pt (100) single crystals and preferentially oriented nanoparticles in neutral media. *Catal Today*. **2013**, 202: 2-11, DOI 10.1016/j.cattod.2012.02.038.
51. Pérez-Gallent, E.; Figueiredo, M. C.; Katsounaros, I.; Koper, M. T. M. Electrocatalytic reduction of Nitrate on Copper single crystals in acidic and alkaline solutions. *Electrochim. Acta*. **2017**, 227, 77-84, DOI 10.1016/j.electacta.2016.12.147.

52. Cunha, M. C. P. M.; Souza, J. P. I. D.; Nart, F. C. Reaction Pathways for Reduction of Nitrate Ions on Platinum, Rhodium, and Platinum-Rhodium Alloy Electrodes. *Langmuir*. **2000**, 16, 771-777, DOI 10.1021/la990638s.

For Table of Contents Use Only

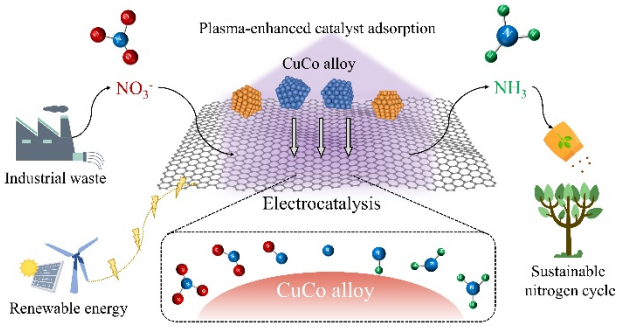

Boosting efficient electrocatalysis through plasma enhanced CuCo alloy-substrate interaction for sustainable nitrogen cycling